Electron-phonon interaction in perovskite nanocrystals in fluorophosphate glass matrix

© M.N. Bataev[1], M.S. Kuznetsova[1], D.V. Pankin[1], M.B. Smirnov[1], S.Yu. Verbin[1], I.V. Ignatiev[1], I.A. Eliseyev[2], V.Yu. Davydov[2], A.N. Smirnov[2], E.V. Kolobkova[3,4]

[1] St. Petersburg State University,
198504 St. Petersburg, Russia
[2] Ioffe Institute of Physics and Technology of the Russian Academy of Sciences,
194021 St. Petersburg, Russia
[3] ITMO University,
199034 St. Petersburg, Russia
[4] St. Petersburg State Technological Institute (Technical University),
190013 St. Petersburg, Russia

E-mail: batae1996@gmail.com

Received May 5, 2023
Revised June 29, 2023
Accepted July 6, 2923

The photoluminescence (PL) spectra of $CsPbBr_3$ perovskite nanocrystals grown in a fluorophosphate glass matrix exhibit phonon replicas of the exciton line. The dependence of intensity of the phonon sidebands are simulated taking into account the difference in the curvature of the excited and ground adiabatic potentials. The Raman spectra of $CsPbBr_3$ nanocrystals are measured. Calculations based on the density functional theory is performed to obtain the spectrum of phonon states of these crystals in the orthorhombic phase. The phonon frequencies observed in the PL and Raman spectra are compared with the calculation results.

Keywords: perovskites, nanocrystals, Raman scattering, phonon replicas, $CsPbBr_3$, fluorophosphate glass.

DOI: 10.21883/0000000000

1. Introduction

Currently, perovskite nanocrystals (NCs) are being extensively studied due to the wide prospects for their practical application [1–4]. Changing the size of nanocrystals and their chemical composition makes it possible to easily vary the energy of optical transitions over the entire visible spectral range. A new class of optical materials are newly synthesized perovskite NCs encapsulated in glass matrices [5–8]. $CsPbX_3$ (X = Cl, Br, I) perovskite nanocrystals synthesized in a fluorophosphate (FP) glass matrix [8] have a number of advantages over colloidal analogues, in particular they have high stability of their physical and, in particular, optical characteristics.

The demonstration of the high quantum yield of photoluminescence (PL) of perovskite NCs has stimulated numerous studies of the energetic structure and crystalline phases of perovskites (see, for example, recent studies [4,9–11] and references in them). It has been found that the bandgap of states is virtually free from impurity levels [9,12], which ensures a high luminescence yield. At the same time, perovskite NCs contain metastable states of excitons with a long lifetime of tens of microseconds [13]. The presence of metastable states results in an interesting effect of anti-Stokes luminescence [14–17]. In addition, these states demonstrate a long-lived spin dynamics, which is promising for the implementation of quantum technologies [13,18–21].

An important role is played by studies of phonon states and exciton-phonon interaction in perovskite NCs [22–25]. Experimental studies of the phonon spectrum at different temperatures of nanocrystals, together with theoretical modeling, make it possible to obtain important information about structural phase transitions.

One of the methods for studying phonons is Raman spectroscopy (RS), which can provide the data to determine the crystal structure and the nature of interatomic interactions in the objects being studied. To get a clearer idea of phonon states, the Raman spectroscopy data should be supplemented by analysis of infrared absorption spectra (IR spectra). This is especially important for crystals with a centrosymmetric structure, which include the compounds investigated in this study. These are polar optical phonons, which are inactive in Raman spectra, that play a decisive role in the mechanism of exciton-phonon interaction [26]. Calculations based on the density functional theory (DFT) make it possible to clarify the information obtained from spectroscopic studies, which helps to interpret phonon spectra.

In this study, the phonon spectrum of the orthorhombic modification of the $CsPbBr_3$ crystal is studied theoretically and experimentally. A comparison of the calculated and experimental Raman spectra made it possible to confirm the structural model of the nanocrystals under study and to correlate the observed spectral peaks with certain phonon states. The calculated IR spectrum made it possible to propose an interpretation of the phonon-related features observed in the PL spectra.

2. Sample fabrication process and characterization of samples

The sample under study is a fluorophosphate (FP) glass with the composition of $60Ba(PO_3)_2-15NaPO_3-12AlF_3-1Ga_2O_3-4Cs_2O-8PbF_2$ (mol%), doped with 3.4 mol% of $BaBr_2$, which was produced by melt quenching. The choice of a fluorophosphate (FP) glass matrix for the formation of $CsPbBr_3$ HCs is motivated by the possibility of injecting high concentrations of halides. The glass was synthesized in a closed glassy carbon crucible at $T = 1000-1050\,^{\circ}C$. About 50 g of mixed powder was melted in the crucible for 20 min. As a result, nearly colorless glass was produced. To produce NCs, the glass was held for 240 min at a glass transition temperature of $T = 400\,^{\circ}C$.

The fact of NCs formation, as well as their sizes were identified using X-ray patterns recorded by a Rigaku X-ray diffractometer. Several weak diffraction peaks were observed, indicating the formation of $CsPbBr_3$ crystalline phases. The NC size was determined by the Scherrer formula: $d = K\lambda(\beta\cos\theta)$, where d is the mean size of ordered (crystalline) domains, which can be less or equal to the size of NC; K is a dimensionless form-factor. Form-factor has a typical value of ~ 0.9 but varies depending on the actual shape of the crystallite. β is line broadening at half maximum intensity in radians, less the instrumental line broadening, θ is Bragg angle in radians. $\lambda = 0.154$ nm is X-ray wavelength. In our case the parameters were as follows: $2\theta = 30.4^{\circ}$, $\theta = 15.2^{\circ}$, $\beta = 0.63^{\circ}$. Based on the analysis of X-ray patterns, the diameter of the NC in the sample under study turned out to be 14.5 nm.

3. Experimental technique and calculation procedure

The non-resonant PL and the spectrum of phonon repetitions in resonant PL was studied using the standard technique of stationary spectroscopy. The sample under study was placed on a cold finger in a closed cycle cryostat, which allowed the samples under study to be cooled to a temperature of $T = 11$ K. The measurements were carried out in the reflection geometry. When studying the non-resonant PL, a laser with a radiation wavelength of $\lambda_{exc} = 405$ nm was used as a light source. The laser radiation was directed at the sample at a small angle to the optical axis so that the reflected beam did not enter the lens aperture in the PL collection channel. To record the PL spectrum, an iHR-550 spectrometer was used (with a focal length of 550 mm, a diffraction grating with 1200 lines/mm). The spectrometer is equipped with a Symphony II CCD camera cooled with liquid nitrogen, which ensures a low noise level. When measuring the resonant PL, the sample was optically excited by a laser with a radiation wavelength of $\lambda_{exc} = 532$ nm, which corresponds to the low-energy edge of the PL band of the $CsPbBr_3$ NC ensemble.

The PL excitation spectra were measured using the same setup. An incandescent lamp with a MDR-4 premonochromator was used as an adjustable radiation source. Due to the fact that light intensity of the lamp depends on the wavelength and the hardware function of the monochromator, the PL excitation spectra were normalized to the intensity of the portion of the lamp spectrum selected by the premonochromator. The use of CCD-camera allowed the excitation spectra to be recorded simultaneously over the entire PL band of the sample under study.

Raman scattering (RS) spectra at a temperature of $T = 7$ K were measured using a T64000 spectrometer equipped with a confocal microscope. A laser with a wavelength of $\lambda_{exc} = 633$ nm was used as an excitation source. The measurements were carried out in the backscattering geometry. The RS of studied samples with $CsPbBr_3$ nanocrystals grown in FP glass are characterized by low signal level. Therefore, the RS spectra of the FP glass matrix without nanocrystals, as well as the spectrum of the air were additionally measured and subtracted from the RS signal of the glass with NCs.

The electronic structure and phonon spectra were calculated using the GGA approximation of the density functional theory with the PBE functional and norm-conserving pseudopotential in the Castep program (Material Studio) [27,28]. The cutoff energy value when building up the plane-wave basis was 1200 eV. To solve the electronic problem, a field self-consistency criterion was set equal to $5 \cdot 10^{-7}$ eV/atom. The k-grid dimension was chosen to be $3 \times 2 \times 3$ (with a step of $0.04\,\text{Å}^{-1}$). The geometry was optimized until residual forces and stresses not exceeding 0.01 eV/Å and 0.02 hPa, respectively, were achieved. For the optimized structure, phonon frequencies were calculated by the linear response method (DFPT) [29].

4. Photoluminescence under resonant excitation

Fig. 1 shows the resonant PL spectrum of a sample with $CsPbBr_3$ NCs measured under resonant excitation to the low-energy edge of the PL band by laser radiation with a photon energy of $E_{exc} = 2.33$ eV ($\lambda_{exc} = 532$ nm). Red arrow indicates the energy of laser radiation. The insert to Fig. 1 shows PL spectrum of the same sample under short-wave excitation with a photon energy of $E_{exc} = 3.06$ eV ($\lambda_{exc} = 405$ nm). In Fig. 1, three phonon repetitions 18 meV apart from each other can be clearly seen on the background of the PL tail, that corresponds to the vibration frequency of $\nu = 150\,\text{cm}^{-1}$.

Fig. 2 shows the PL excitation spectra measured at different PL detection energies, $E_{det} = 2.375$, 2.380, 2.385 eV, corresponding to the high-energy edge of the PL band (see the inset in Fig. 1). As can be seen in the figure, several broad peaks are observed in the studied spectral region.

The leftmost peak is shifted to the left side of the spectrum as the energy of the detected photons E_{det} increases. This feature of the spectrum is presumably associated with the resonant excitation of excitons into the second size-quantized state in the NCs under study. As E_{det} increases, the size of the NCs decreases in the subensemble from which the PL is recorded. Accordingly, the energy of the first and subsequent size-quantized exciton levels increases, as well as does the energy gap between them, which explains the shift of the observed peak in the PL excitation spectrum.

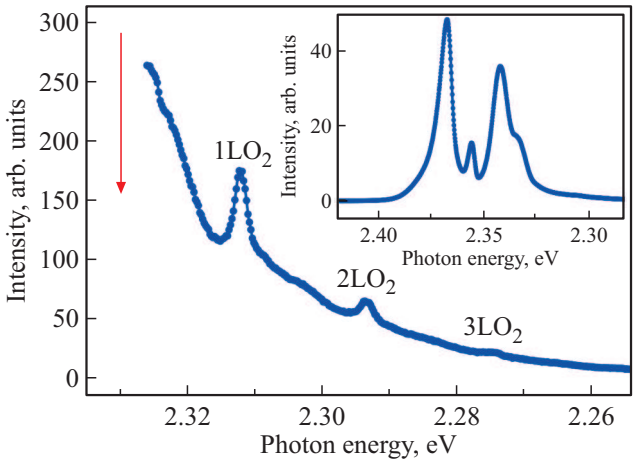

Figure 1. The resonant PL spectrum under excitation of $CsPbBr_3$ NCs by laser radiation with a photon energy of $E_{exc} = 2.33$ eV ($\lambda_{exc} = 532$ nm). Red arrow indicates the energy of photons of the optical excitation. A number of LO phonon repetitions corresponding to frequencies that are multiples of 150 cm^{-1} (18 meV) can be seen on the background of the PL tail. The inset to the figure shows the PL spectrum measured under excitation by laser radiation with a photon energy of $E_{exc} = 3.06$ eV ($\lambda_{exc} = 405$ nm). The measurements were taken at a temperature of $T = 11$ K.

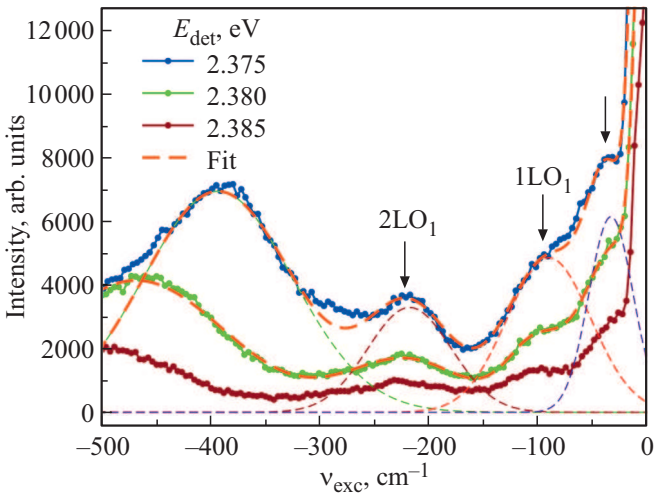

Figure 2. PL excitation spectra measured at different PL detection energies given in the legend. The horizontal axis shows the difference between the detection energies of PL and excitation light photons in reciprocal centimeters. The intense signal observed in the region < 25 cm^{-1} is associated with the scattered radiation from the light source. The dashed curves show the decomposition of the spectrum into Gaussian contours and the fitting of these spectra by the sum of these contours. $T = 11$ K. (The colored version of the figure is available on-line).

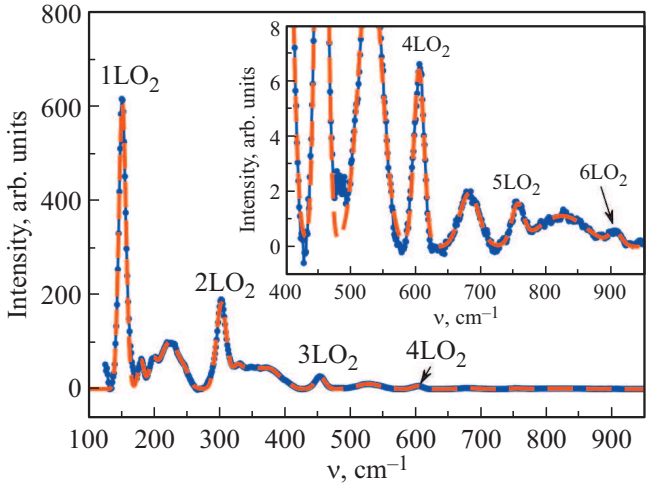

Figure 3. Spectrum of phonon repetitions of $CsPbBr_3$ NCs under resonant excitation of PL, $E_{exc} = 2.33$ eV ($\lambda_{exc} = 532$ nm). The smooth PL component is subtracted. Dashed line shows the fitting by sum of Gaussian contours. The inset shows 100 times zoomed in the 400–950 cm^{-1} part of the spectrum. $T = 11$ K.

Other features of the PL excitation spectrum observed in Fig. 2 (shown with arrows) at frequencies of $\nu_{exc} \approx -217$, -107, -39 cm^{-1} retain their positions nearly unchanged relative to E_{det}. Therefore, we assume that these features are due to exciton-phonon transitions in the PL excitation spectra, i. e. simultaneous production of exciton and phonons with the above-specified frequencies. In this case, the frequency of 107 cm^{-1} corresponds to the production of one LO-phonon, and the frequency of 217 cm^{-1} corresponds to the production of two LO-phonons. It should be noted that the LO phonon frequency in the excited state of the electronic system ($\nu_1 \approx 108$ cm^{-1}) is significantly lower than that of the LO phonon in the ground state ($\nu_2 = 150$ cm^{-1}). This indicates a significant difference in the curvature of the adiabatic potentials in the ground electronic state and excited electronic state.

5. Spectrum of phonon states

To study in detail the phonon spectrum in the lower state of the electronic subsystem, we conducted a study of the resonant PL with a long signal accumulation time, which provided a dynamic range of 3 decimal orders. Fig. 3 shows the measured spectrum from which the smooth component of the PL signal was subtracted. Thanks to the accumulation of the signal, we were able to detect the 6 highest-frequency phonon repetitions corresponding to the

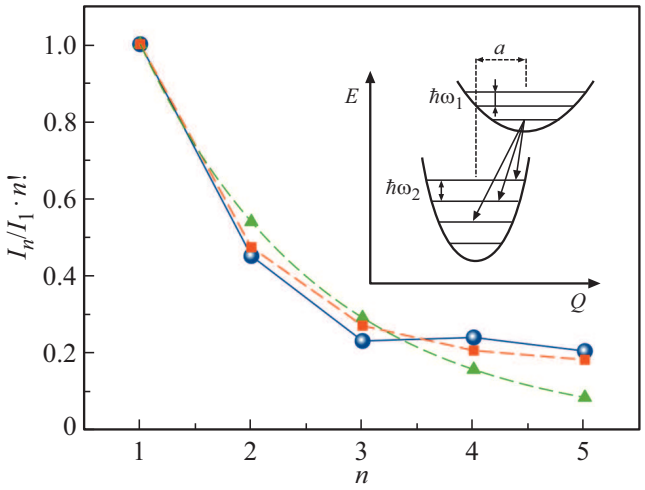

Figure 4. $I_n/I_1 \cdot n!$ values as a function of phonon replica number. Blue dots show experimentally obtained values, green triangles show approximation in the Huang–Ries model ($S = 0.54$), red squares show the calculation within the model [35]. The inset shows the diagram of adiabatic potentials and observed optical transitions. The a parameter describes the shift of the minima of the adiabatic potentials.

frequency of $\nu_2 = 150\,\mathrm{cm}^{-1}$. The theoretical calculation described below allows us to attribute this phonon state to a longitudinal optical (LO) vibration corresponding to antiphase displacements of cations and anions.

Blue dots in Fig. 4 show the dependence of the intensity of exciton-phonon transitions normalized to the intensity of the first peak and multiplied by $n!$, where n is the number of the phonon replica. This allows the intensities of all peaks within the same decimal order to be shown. The inset to Fig. 4 schematically shows the Franck–Condon model [30–32], within which the behavior of phonon replicas is analyzed. This model uses an adiabatic approximation to separate electronic and vibrational degrees of freedom and a parabolic approximation for adiabatic potentials. The potential minima are shifted relative to each other by a certain value of a. The curvature of the potentials is also different, which describes the difference in vibration frequencies measured in the resonant PL and excitation PL spectra. The exciton-phonon transitions observed in the experiment are shown in the diagram by arrows.

To theoretically model the intensity of phonon replicas, the one-dimensional Schrödinger equation for a harmonic oscillator is solved [33]:

$$-\frac{-\hbar^2}{2m}\frac{\partial^2}{\partial x^2}\psi_n(x) + \frac{m\omega^2 x^2}{2}\psi_n(x) = E_n\psi_n(x). \qquad (1)$$

Here it is represented in the standard notation. Let us reduce this equation to a dimensionless form by replacing the variable:

$$Q = \sqrt{\frac{m\omega}{\hbar}}\,x. \qquad (2)$$

Then the Schrödinger equation takes the following form:

$$\frac{\partial^2}{\partial Q^2}\psi_n(Q) + \left(\frac{2E_n}{h\omega} - Q^2\right)\psi_n(Q) = 0. \qquad (3)$$

As a result of solving the Schrödinger equation, the wave functions of vibrational states are obtained:

$$\psi_n(Q) = \left(\frac{1}{\pi}\right)^{1/4}\frac{1}{\sqrt{2^n n!}}\exp\left(\frac{Q^2}{2}\right)H_n(Q), \qquad (4)$$

where $H_n(Q)$ are Hermite polynomials.

The curvature parameter of adiabatic potentials is determined by the following ratio:

$$\beta_{1,2} = \frac{m\omega_{1,2}^2}{2}, \qquad (5)$$

where $\omega_{1,2} = 2\pi\nu_{1,2}$. Let us introduce the ratio of curvature of adiabatic potentials, $\beta = \beta_1/\beta_2 = \omega_1^2/\omega_2^2$. We will assume that wave function (4) describes vibrational states in the lowest electronic state. The representation for the wave function of the upper state is obtained by replacing the variable, $Q_1 = \sqrt[4]{\beta}(Q - a)$, taking into account the shift of the upper adiabatic potential and the change in its curvature. Taking into account the change in normalization, the vibrational wave function in the upper state has the following form:

$$\psi_n'(Q) = \sqrt[4]{\frac{\sqrt{\beta}}{\pi}}\frac{1}{\sqrt{2^n n!}}\exp\left(-\frac{Q_1^2}{2}\right)H_n(Q_1). \qquad (6)$$

The PL spectra show optical transitions between the lowest vibrational state in the upper electronic state and various vibrational states in the ground electronic state. The intensities of these transitions in the Franck–Condon model are determined by the square of the integral of vibrational wave functions overlap:

$$I_n = \left|\int_{-\infty}^{-\infty}\psi_0'(Q)\psi_n(Q)dQ\right|^2. \qquad (7)$$

Let us first consider the simplest case, the Huang-Ries model [34], where it is assumed that the curvature of the lower and upper adiabatic potentials is the same ($\beta = 1$) and, accordingly, $\omega_1 = \omega_2$. In this model, the integrals of overlap are easily calculated analytically, and the expression for the intensity of transitions takes the following simple form:

$$I_n = e^{-S}\frac{S^n}{n!}, \qquad (8)$$

where $S = a^2/2$. Fig. 4 shows the fitting of the experiment by the $I_n/I_1 \cdot n! = S^{n-1}$ dependence, which follows from the above expression. The optimal value of the model parameter determined by the least square method is $S = 0.54$ ($a = 1.04$). It can be seen that this model proves a very rough approximation of the intensity behavior of phonon replicas. This was to be expected, because $\omega_1 \neq \omega_2$ as

it follows from the experiment on resonant PL and PL excitation spectra.

For a more rigorous description of the intensities of phonon replicas, we calculated the overlap integrals included in expression (7), taking into account different curvatures of adiabatic potentials ($\beta = \beta_1/\beta_2 \neq 1$). In this case, analytical formulae can also be obtained for expression (7). They are given in [35] for the first few vibrational states. Fig. 4 shows the dependence obtained within this model for the optimal values of its parameters: $a = 0.7$ and $\sqrt{\beta} = \omega_1/\omega_2 = 0.8$. It can be seen that this model provides a more accurate description of the experiment. However, the resulted frequency ratio is somewhat different from the ratio obtained from the spectra of PL excitation and resonant PL ($\sqrt{\beta} = \omega_1/\omega_2 = 0.7$). The discrepancy is probably due to the error in determining the ω_1 frequency and the ratio of phonon repetition intensities, respectively, as well as to the approximation nature of the model [35].

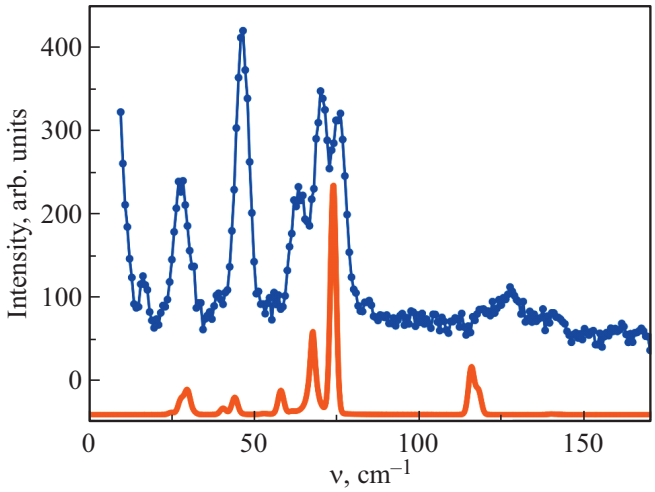

Figure 5. RS spectrum of $CsPbBr_3$ NC (blue line), measured at a temperature of 7 K, and the calculated spectrum of phonons for the orthorhombic phase (red line).

6. Theoretical modeling of phonon spectra

The first stage of the theoretical study of phonon states was the search for a structure corresponding to the minimum energy of the electronic subsystem. Such a structure was found as a result of complete (both with respect to the cell parameters and with respect to atomic positions) optimization of the geometry of the orthorhombic modification of $CsPbBr_3$ with space group *Pnma* and four formula units in the cell. Theoretical estimates of the cell parameters (8.402, 11.756, and 8.179 Å) turned out to be close to those found experimentally (8.186, 11.659, and 8.098 Å) [36].

Then the centerband phonon states were calculated. All modes were divided into irreducible representations of the symmetry group. For all inversion-invariant modes (so-called *g*-modes), their intensities in the RS spectra were determined. According to the group theory, for the orthorhombic modification, 24 active RS modes are predicted for the Γ-point: $7A_g + 5B_{1g} + 7B_{2g} + 5B_{3g}$. The calculated depolarized RS-spectrum of the orthorhombic phase of $CsPbBr_3$ is shown in Fig. 5. The half-height line width is taken equal to 2 cm^{-1}.

It can be seen that two intense lines at frequencies of 67 and 74 cm^{-1} are dominating in the calculated spectrum. The corresponding phonons with A_g and B_{2g} symmetry are bending vibrations of $PbBr_6$ octahedra. In the experimental RS spectrum, which is also shown in Fig. 5, these lines can be associated with a double peak with maxima at 70 and 76 cm^{-1}.

The high-frequency line near 115 cm^{-1} is associated with A_g and B_{3g} symmetry modes corresponding to asymmetric stretching vibrations localized in Pb−Br−Pb bridges. In the experimental RS spectrum, these lines can be associated with a peak with a broad maximum at about 125 cm^{-1}. For three less intense lines with frequencies of 30, 44 and 58 cm^{-1}, associated with scattering by phonons of A_g symmetry, corresponding peaks can be found in the experimental RS spectrum as well.

It should be noted that there are discrepancies between the predicted line intensities in the calculated RS spectrum and those obtained experimentally. Possible reasons for these differences may be the quantum size effect and the influence of the glass matrix.

Modes, which are anti-invariant to inversion (so-called *u*-modes), are inactive in the RS spectrum but active in IR spectra. According to the group theory, for the Γ-point in the IR spectra, 28 active modes are predicted: $10B_{1u} + 10B_{2u} + 8B_{3u}$. For all transverse optical (TO) modes, we calculated the oscillator forces and determined the spectrum of the corresponding longitudinal optical (LO) modes. The intensities in the IR absorption spectra were calculated for all TO and LO modes.

It has been shown in a number of studies [37,38], that electron-phonon and exciton-phonon interactions in a $CsPbBr_3$ crystal are mainly determined by the scattering of carriers by LO phonons (the so-called Froehlich mechanism). Therefore, having defined our next task to be the interpretation of PL spectra, we paid special attention to the spectrum of LO modes. For B_{1u}, B_{2u}, and B_{3u} representations polarized in different crystallographic directions, frequencies and shapes of LO modes were calculated and their IR intensities were determined. We used this IR spectrum to model phonon replicas in the PL spectra.

According to our calculations, in each direction there is only one, the most high-frequency LO-mode in the set that has a noticeable IR intensity. Therefore, a conclusion can be made that the main 1LO−6LO phonon replicas shown in Fig. 3 are most likely formed exactly by these modes. The calculated frequency of this vibration is $\nu \approx 140$ cm^{-1},

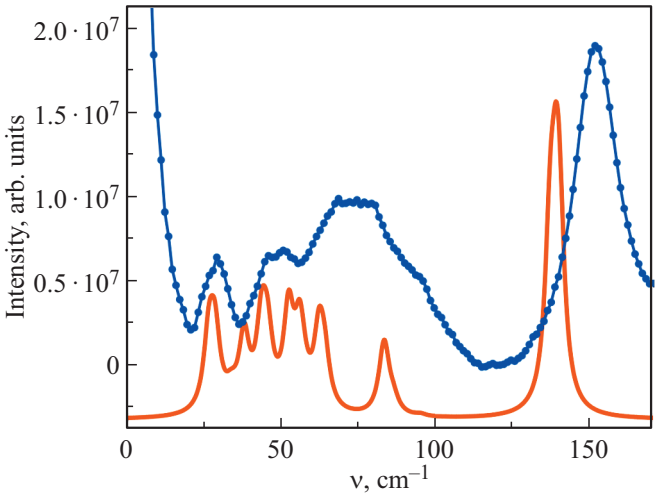

Figure 6. Phonon repetitions spectrum between 1LO and 2LO peaks. The red curve shows the calculated IR absorption spectrum summed over different directions of the wave vector **k**.

which is well consistent with the experimental frequency of $\nu = 150\,\mathrm{cm}^{-1}$. However, broad additional features are observed between the main phonon replicas in the experimentally measured PL spectrum. Presumably, their presence is associated with the manifestation of other, less active LO phonons. Fig. 6 shows the part of the PL spectrum between the first and the second phonon replicas. The position of the first phonon repetition is taken as the starting point. In the single-crystal case, the spectrum of phonon repetitions depends on the polarization of the exciting light and the orientation of the crystal relative to the radiation. Accordingly, when interpreting such a spectrum, we should use LO phonons with a certain polarization. Due to the fact that the object of our study is an ensemble of disordered nanocrystals grown in glass, the spectrum of phonon repetitions neither depends on polarization nor on orientation of the sample. To interpret such a spectrum, the spectrum of LO phonons should be averaged over the polarization direction. Such a spectrum, calculated for the orthorhombic phase $CsPbBr_3$, is shown with the red curve in Fig. 6. The half-height width of phonon lines is taken equal to $2\,\mathrm{cm}^{-1}$.

It can be seen that, in general, the pattern of the spectrum plotted on the basis of the calculation results reflects the frequency distribution of features observed in the experimental PL spectrum.

7. Conclusion

Phonon repetitions in the resonant photoluminescence spectrum of $CsPbBr_3$ nanocrystals were found and experimentally studied. Behavior of the integral intensity of phonon replicas depending on the number has been theoretically modeled, which makes it possible to estimate the curvature ratio between the excited and ground adiabatic potentials for vibrational states in the $CsPbBr_3$ NCs. The modeling results are further confirmed by experimental measurements of phonon frequencies in the excited and ground electronic states of the system. According to the results of modeling the spectrum of polar phonons, regardless of the crystal orientation, only one frequency is most actively manifested in the PL spectra, which is confirmed experimentally. A comparison of the results of an experimental study of Raman scattering spectra and calculations suggests that $CsPbBr_3$ nanocrystals grown in a fluorophosphate glass matrix have an orthorhombic crystal lattice. Discrepancies with the theory may be due to the effect of size quantization and the influence of the glass matrix.

Funding

The authors would like to thank St. Petersburg State University for the financial support provided through grants No. 19850494030557 and No. 94271404 and the state assignment of the Ioffe Institute of Physics and Technology (0040-2019-0006).

Conflict of interest

The authors declare that they have no conflict of interest.

References

[1] L. Protesescu, S. Yakunin, M.I. Bodnarchuk, F. Krieg, R Caputo, C.H. Hendon, R.X. Yang, A. Walsh, M.V. Kovalenko. Nano Lett., **15** (6), 3692 (2015).
[2] P. Ramasamy, D.-H. Lim, B. Kim, S.-H. Lee, M.-S. Lee, J.-S. Lee. Chem. Commun., **52**, 2067 (2016).
[3] X. Li, Y. Wu, S. Zhang, B. Cai, Y. Gu, J. Song, H. Zeng. Advanced Functional Mater., **26** (15), 2435 (2016).
[4] M.A. Becker, R. Vaxenburg, G. Nedelcu, P.C. Sercel, A. Shabaev, M.J. Mehl, J.G. Michopoulos, S.G. Lambrakos, N. Bernstein, J.L. Lyons, T. Stoferle, R.F. Mahrt, M.V. Kovalenko, D.J. Norris, G. Raino, A.L. Efros. Nature, **553**, 189 (2018).
[5] P. Li, C. Hu, L. Zhou, J. Jiang, Y. Cheng, M. He, X. Liang, W. Xiang. Mater. Lett., **209** (C), 483 (2017).
[6] S. Liu, Y. Luo, M. He, X. Liang, W. Xiang. J. Eur. Ceramic Soc., **38** (4), 1998 (2018).
[7] Y. Ye, W. Zhang, Z. Zhao, J. Wang, C. Liu, Z. Deng, X. Zhao, J. Han. Adv. Opt. Mater., **7** (9), 1801663 (2019).
[8] E. Kolobkova, M. Kuznetsova, N. Nikonorov. J. Non-Cryst. Sol., **563**, 120811 (2021).
[9] A.O. Murzin, N.I. Selivanov, V.O. Kozlov, I.I. Ryzhov, T. Miyasaka, A.V. Emeline, Y.V. Kapitonov. Adv. Opt. Mater., **9** (18), 2001327 (2021).
[10] T. Yamada, T. Handa, Y. Yamada, Y. Kanemitsu. J. Phys. D: Appl. Phys., **54** (38), 383001 (2021).
[11] S. Liu, A.R. DeFilippo, M. Balasubramania n, Z. Liu, S.G. Wang, Y.-S. Chen, S. Chariton, V. Prakapenka, X. Luo, L. Zhao, J.S. Martin, Y. Lin, Y. Yan, S.K. Ghose, T.A. Tyson. Adv. Sci., **8** (18), 2003046 (2021).
[12] R. Brakkee, R.M. Williams. Appl. Sci., **10** (9), 3061 (2020).

[13] V.V. Belykh, M.L. Skorikov, E.V. Kulebyakina, E.V. Kolobkova, M.S. Kuznetsova, M.M. Glazov, D.R. Yakovlev. Nano Lett., **22** (11), 4583 (2022).
[14] X. Ma, F. Pan, H. Li, P. Shen, C. Ma, L. Zhang, H. Niu, Y. Zhu, S. Xu, H. Ye. J. Phys. Chem. Lett., **10** (20), 5989 (2019).
[15] A. Granados del'Aguila, T.T.H. Do, J. Xing, J.J. Wen, J.B. Khurgin, Q. Xiong. Nano Res., **13**, 1962 (2020).
[16] W. Zhang, Y. Ye, C. Liu, J. Wang, J. Ruan, X. Zhao, J. Han. Adv. Opt. Mater., **9** (6), 2001885 (2021).
[17] M.N. Kuznetsova, Maria S. and Bataev, M.A. Chukeev, N.D. Rostovtsev, S.Y. Verbin, I.V. Ignatiev, V.Y. Davydov, A.N. Smirnov, I.A. Eliseev, E.V. Kolobkova. Opt. Spectrosc., **130** (11), 1472 (2022).
[18] S. Strohmair, A. Dey, Y. Tong, L. Polavarapu, B.J. Bohn, J.Feld-mann. Nano Lett., **20** (7), 4724 (2020).
[19] M.J. Crane, L.M. Jacoby, T.A. Cohen, Y. Huang, C.K. Luscombe, D.R. Gamelin. Nano Lett., **20** (12), 8626 (2020).
[20] P.S. Grigoryev, V.V. Belykh, D.R. Yakovlev, E. Lhuillier, M. Bayer. Nano Lett., **21** (19), 8481 (2021).
[21] E. Kirstein, N.E. Kopteva, D.R. Yakovlev, E.A. Zhukov, E.V. Kolobkova, M.S. Kuznetsova, V.V. Belykh, I.A. Yugova, M.M. Glazov, M. Bayer, A. Greilich. Nature Commun., **14** (699) (2023).
[22] R. Saran, A. Heuer-Jungemann, A.G. Kanaras, R.J. Curry. Adv. Opt. Mater., **5** (17), 1700231 (2017).
[23] Y. Guo, O. Yaffe, T.D. Hull, J.S. Owen, D.R. Reichman, L.E. Brus. Nature Commun., **10** (1), 1175 (2019).
[24] Y. Yamada, Y. Kanemitsu. NPG Asia Mater., **14** (1), 48 (2022).
[25] K. Cho, H. Tahara, T. Yamada, H. Suzuura, T. Tadano, R. Sato, M. Saruyama, H. Hirori, T. Teranishi, Y. Kanemitsu. Nano Lett., **22** (18), 7674 (2022).
[26] C.M. Iaru, A. Brodu, N.J.J. van Hoof, S.E.T. ter Huurne, J. Buhot, F. Montanarella, S. Buhbut, P.C.M. Christianen, D. Vanmaekelbergh, C. de Mello Donega, J.G. Rivas, P.M. Koenraad, A.Yu. Silov. Nature Commun., **12** (1), 5844 (2021).
[27] S.J. Clark, M.D. Segall, C.J. Pickard, P.J. Hasnip, M.I.J. Probert, K. Refson, M.C. Payne. Zeitschriftf'ur Kristallogr. — Crystalline Mater., **220** (5–6), 567 (2005).
[28] K. Refson, P.R. Tulip, S.J. Clark. Phys. Rev. B, **73**, 155114 (2006).
[29] X. Gonze, C. Lee. Phys. Rev. B, **55**, 10355 (1997).
[30] J. Franck, E.G. Dymond. Trans. Faraday Soc., **21**, 536 (1926).
[31] E. Condon. Phys. Rev., **28**, 1182 (1926).
[32] P. Atkins. *Molecular quantum mechanics* (Oxford Univ. Press, Oxford, 2005).
[33] L.D. Landau, L.M. Lifshitz. *Quantum Mechanics Non-Relativistic Theory*. 3rd edn (Pergamon Press Ltd, 1965) v. 3, 67.
[34] K. Huang, A. Rhys, N.F. Mott. Proc. Royal Society of London. Ser. A. Math. Phys. Sci., **204** (1078), 406 (1950).
[35] V.S. Krivobok, S.N. Nikolaev, V.S. Bagaev, S.I. Chentsov, E.E. Onishchenko, A.A. Pruchkina. JETP Lett., **114** (2), 98 (2021).
[36] M. Szafrański, A. Katrusiak, K. Ståhl. J. Mater. Chem. A, **9**, 10769 (2021).
[37] C.M. Iaru, J.J. Geuchies, P.M. Koenraad, D. Vanmaekelbergh, A.Y. Silov. ACS Nano, **11** (11), 11024 (2017).
[38] X. Zhou, Z. Zhang. AIP Advances, **10** (12), 125015 (2020).